Pressure Sensitive Paint Measurements on a Hemispherical Turret

Matthew Kalensky[*a], Stanislav Gordeyev[a], Brian Catron[a],
Eric J. Jumper[a], and Matthew Kemnetz[b]

[a] *University of Notre Dame, Notre Dame, IN, 46556*
[b] *U.S. Air Force Research Laboratory, Kirtland Air Force Base, New Mexico, 87117*

ABSTRACT

Surface pressure measurements were taken on a hemisphere-on-cylinder turret in a wind tunnel using pressure sensitive paint and fast response pressure transducers. Four different turret protrusion distances were tested to study the characteristics of the unsteady pressure field on the backside and wake of the turret. Proper orthogonal decomposition was used to identify the dominant spatial surface pressure modes acting on the turret in this parametric study. It was found that the further the turret protruded into the freestream flow, the more the surface pressure field became dominated by spanwise antisymmetric surface pressure distributions resulting from anti-symmetrical vortex shedding at a normalized frequency of approximately $St_D=0.2$. For the case of the partial hemisphere, this anti-symmetrical vortex shedding was essentially absent, insinuating that at some protrusion distance, the surface pressure environment on the turret fundamentally changes. The normalized net force rms was calculated on the turret for each configuration. It was found that the greater the turret protrusion, the greater the net force acting in the spanwise direction.

Keywords: Turret, hemisphere-on-cylinder, wind tunnel, pressure sensitive paint, beam control, directed energy, proper orthogonal decomposition, surface pressure measurements

1. INTRODUCTION

The fluid mechanics of hemispherical shaped geometries has been heavily researched in recent years. Many experimental and computational studies were conducted in the early 1980s to early 1990s to investigate the fluid mechanics of hemispheres and hemisphere-on-cylinder geometries due to their relevance in applications such as the design of dome shaped buildings, dome shaped aircraft sensors, optical communications, and directed energy beam director design[1-5]. Directed energy and optical communications systems use hemispherical turrets for their advantageous field of regard. When a turret is mounted on a high-speed aircraft, the hemispherical geometries protrusion into the freestream flow creates a complicated turbulent wake region, which degrades the performance of airborne mounted optical systems at backward looking angles. Consequently, the fluidic and aero-optical properties of turrets have continued to be extensively studied both experimentally and numerically in the last decade[5-15]. In addition to the aero-optical induced distortions associated with turrets, the complicated fluid-structure interaction associated with the turret protruding into the freestream also introduces problems. Despite engineers' best efforts, a turret is not a rigid body. Therefore, the elastic motion of the turret imposes a shaking or vibration into the system and onto the associated system components. One culprit for the mechanical contamination imposed onto the turret is the unsteady surface pressure field associated with the complicated turbulent flow structures around and behind the turret[5,15]. For applications such as airborne directed energy systems, the degree of degradation to optical system performance due to mechanical contamination ultimately depends on the architecture of the beam director itself. However, the unsteady pressure field depends solely on the shape and protrusion of the geometry into the incident flow and the incoming Mach number. Therefore, it is beneficial to study the unsteady surface pressure field to better understand the local forces acting on the body. In the past, arrays of fast response pressure transducers have been used to do so. Although fast response pressure transducers have exceptional response, they're sparsely placed over surfaces, making it difficult to resolve the fine details of a complicated surface pressure field. Recently, fast-response pressure sensitive paint (PSP) has been used to study surface pressure fields for a variety of applications. PSP is able to resolve the flow-field three-dimensionally, alleviating the issue of only having sparsely placed arrays of pressure sensors. The response of PSP is much slower than traditional pressure transducers but even this has improved greatly in recent years. In the work presented here, wind tunnel tests are conducted where PSP is coupled with several fast response Kulite

Email | *mkalensk@nd.edu phone | (574) 631-8349

pressure transducers to study the surface pressure field on different hemisphere and hemisphere-on-cylinder turret geometries at various Mach numbers. Ultimately, the goal of this work is the better understand the local forces acting on the turret resulting from the complicated turbulence environment around these geometries. These findings will better help system designers for airborne directed energy or optical communications systems.

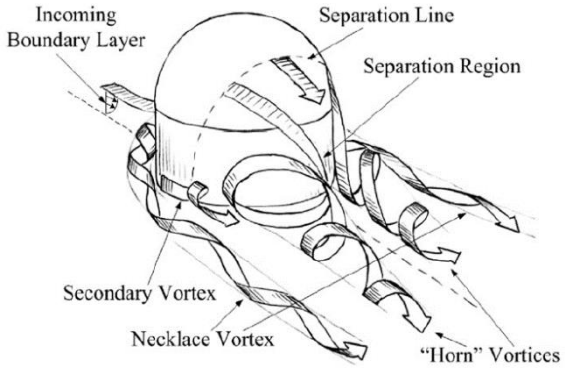

Figure 1. Subsonic flow around a hemispherical turret[5].

As previously mentioned, the fluid mechanics of hemispherical geometries in freestream flow has been studied extensively in the last decade. Some of the major findings can be briefly summarized as follows and are visualized in Fig. 1. Subsonic flow stagnates at the lower frontal portion of the turret and creates a coherent vortical structure which extends around the turret and then convects downstream. This structure is referred to as the "necklace" vortex. The fluid incident to the upper frontal part of the turret stagnates, and then accelerates over the top of the hemispherical body. This frontal region of the turret is fairly steady. The fluid which convects over the top of the turret eventually separates due to the adverse pressure gradient. For Reynolds numbers greater than 3×10^5, separation typically occurs around 120° relative to the incoming freestream however this angle is dependent on other factors[5]. Once the flow separates, a shear layer forms between the freestream flow over the turret and the separation region directly downstream of the turret body. Symmetrical, counterrotating vortices, referred to as "horn" vortices form in this wake region as illustrated in Fig. 1. At low Mach numbers, the turbulent structures in this wake are more coherent. As Mach number increases, the horn vortices lose their symmetry and additional vortices begin shedding off the back of the turret[5]. Based on this description, it is obvious that Mach number and turret geometry play a large role in the resultant turbulence environment around a turret. In addition to varying Mach number, four turret configurations corresponding to varying protrusion distances were tested in these experiments.

2. EXPERIMENTAL SETUP

As described above, surface pressure measurements of various hemispherical turret geometries were collected in a wind tunnel at varying Mach numbers. The turret used in the experiments presented in this work had a diameter of D=0.30 m (12 in). Greater detail on the wind tunnel facility, turret geometries, PSP, and other diagnostic instrumentation are discussed in the sections below.

2.1 Wind Tunnel Setup and Turret Geometries

Wind tunnel tests were performed at the University of Notre Dame's White Field Mach 0.6 wind tunnel facility. This wind tunnel has a 0.91 by 0.91 m (3 by 3 ft) test section capable of producing Mach numbers up to approximately 0.6. The facility is particularly useful for these experiments since the dynamic pressures in the tunnel are close to the dynamic pressures seen in real transonic flight environments. Turret geometries of four different protrusion distances, H, into the freestream flow were tested. These different protrusions were H=0.07 m (2.75 in), 0.15 m (6 in), 0.19 m (7.5 in), and 0.27 m (10.5 in) and are referred to as "partial hemisphere," "hemisphere," "hemisphere on partial cylinder," and "hemisphere on full cylinder," respectively. For protrusion distances greater than the radius of the hemisphere portion of the turret, the cylindrical mount also protruded into the flow. These so called "hemisphere on cylinder" configurations (H = 0.19 m and 0.27 m) have also been previously researched[5]. For all configurations, Mach numbers 0.3, 0.4, and 0.5 are tested, and tunnel temperature, static and total pressures are also recorded.

2.2 Pressure Sensitive Paint and Associated Setup

Pressure sensitive paint (PC-PSP) was applied to the hemispherical pressure turret and the cylinder it sits on, as well as the wind tunnel mounting plate downstream of the turret centerline. The PC-PSP was applied with a thickness of approximately 100 μm. Greater details on the PSP and application process can be found in Refs [16,17]. The turret and associated components were mounted onto a raisable table allowing the turret to be lifted and lowered with ease. Eight ultraviolet (UV) lights were installed, four on either side of the test section in order to illuminate the turret during testing. The UV lights were aimed through quartz window inserts to minimize reflection losses. Two high speed Phantom cameras, v1611 and v2512, were used to simultaneously image each side of the turret. These cameras were time synced with each

other, as well as the fast response pressure transducers also installed on the setup. The cameras collected images at 3 kHz. Filters were also placed in front of each camera to ensure that only the PSP signal was measured. An image of the experimental setup can be seen in Fig. 2.

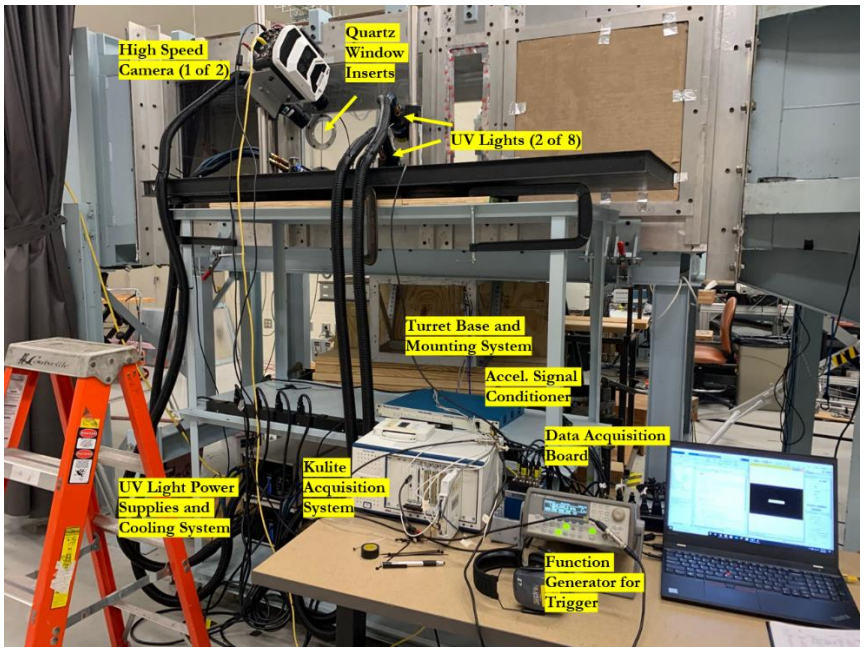

Figure 2. Experimental setup on outward side of the test section.

2.3 Fast Response Pressure Transducer Measurements

In addition to PSP image measurements, simultaneous surface mounted pressure transducer measurements are also collected in order to perform the in-situ PSP calibration. Four Kulite XT-140 pressure transducers were installed on the hemispherical turret. This type of pressure transducer was selected for its high sampling capability and suitable pressure range. The four Kulites were placed on the top, back, and one on each side of the turret in the spanwise direction and each sensor was referenced to the ambient lab conditions. The locations of these Kulites mounted on the turret surface can be seen in Fig. 3. These fast response pressure transducers were sampled at 30 kHz and as mentioned before, were time synced with camera measurements. An image of the hemisphere on full cylinder configuration illuminated in the wind tunnel can be seen in Fig. 4.

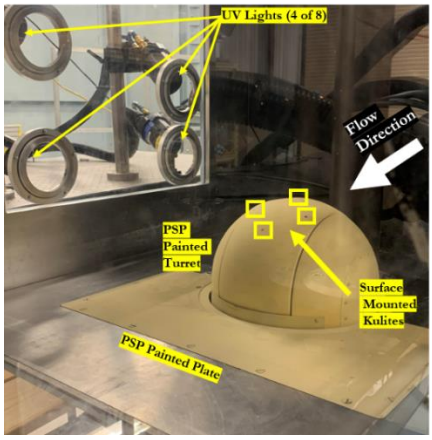

Figure 3. Kulite locations on turret mounted in wind tunnel.

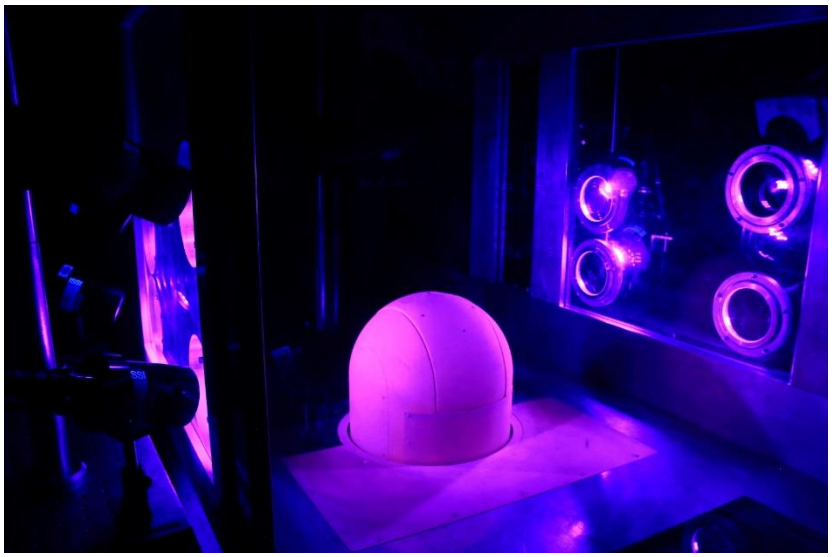

Figure 4. Hemisphere on full cylinder painted with PSP and illuminated with UV lights in the wind tunnel facility.

3. DATA REDUCION AND PROCESSING

3.1 PSP Processing

3.1.1 Calibration

Intensity variations, I, of the PSP are related to instantaneous local static pressure fluctuations, P, by the Stern-Volmer equation,

$$\frac{I_{REF}}{I} = A + B\frac{P}{P_{REF}}. \tag{1}$$

Here, I_{REF} is an intensity reference image, which for these experiments was an average of no flow images of the turret with the UV lights on for each configuration. The variables A and B are experimentally determined constants and P_{REF} was the ambient lab pressure. The constants A and B are found by performing a calibration using the Kulite pressure measurements. Using the intensity fluctuations in proximity to each Kulite for varying Mach numbers, a calibration curve is generated. This was done for both cameras and all turret configurations, the results of which can be seen in Fig. 5. A linear curve fit is applied to the data and the calibration constants represent the slope and offset of this fit. These calibration equations allow the collected intensity images to be converted into pressure fields.

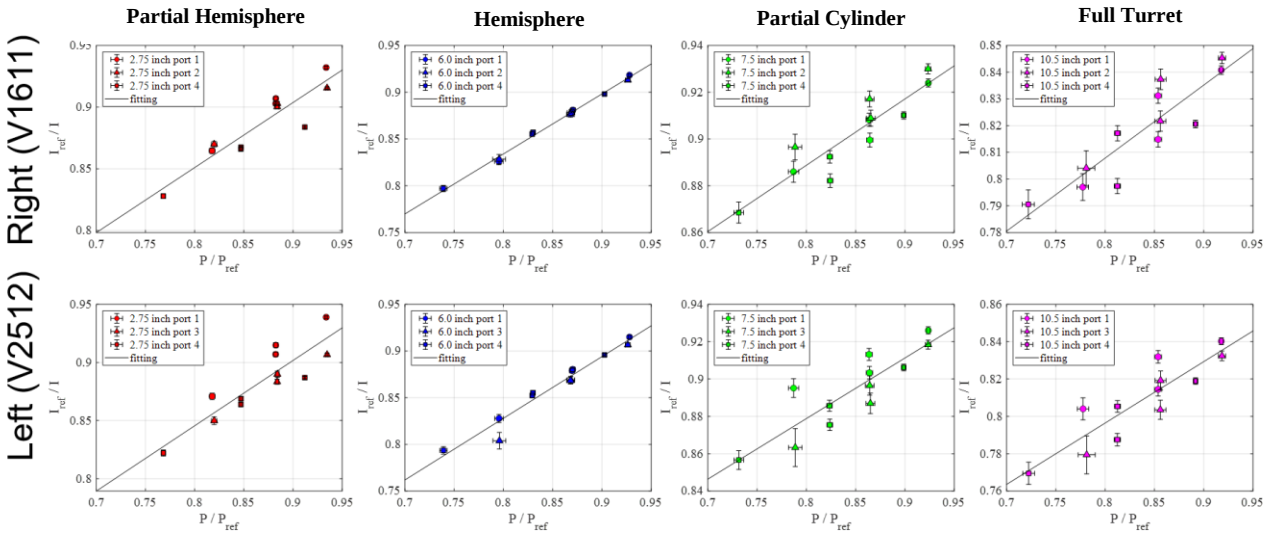

Figure 5. Calibration curves from in-situ calibration for both cameras and all turret configurations.

3.1.2 Surface Pressure Reconstruction

The PSP measurements were collected by way of two high speed cameras collecting synchronized images of both sides of the turret in the wind tunnel. Ultimately, it is desirable to study the full three-dimensional surface pressure field of the turret. Since cameras collect two-dimensional images, a perspective matrix transformation (PMT) technique is employed to project the two-dimensional image measurements into a three-dimensional intensity field[18,19]. Given that some information about where objects within the images are located is known, the PMT establishes a relationship between a three-dimensional physical space point, (X_0, Y_0, Z_0), and an image point (X_1, Y_1), using the following transformation,

$$\begin{bmatrix} a \\ b \\ w \end{bmatrix} = PTM * \begin{bmatrix} X_0 \\ Y_0 \\ Z_0 \\ 1 \end{bmatrix}, \qquad X_1 = \frac{a}{w};\ Y_1 = \frac{b}{w}. \tag{2}$$

Here, PTM is a matrix calculated based on the camera's location and perspective. In order to generate a PTM for each camera, a mask consisting of *x*-,*y*-, *and z*-points at known locations is placed around the turret. Once the PTM is calculated for both cameras, an associated pixel location can be extracted for a given (X_0, Y_0, Z_0) point within the field of interest. A calibration image with the (X_0, Y_0, Z_0) locations of interest projected onto it is shown in Fig. 6. Here, the locations of interest for extracting an (X_1, Y_1) intensity value are represented as green dots[15].

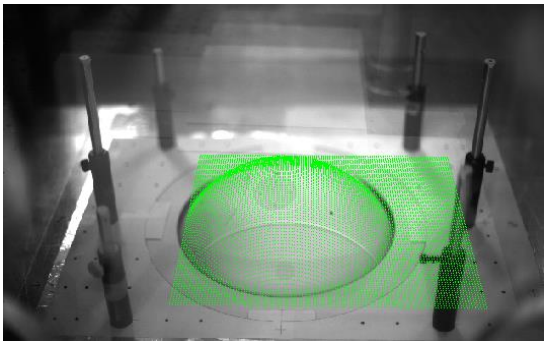

Figure 6. Calibration image with physical space locations of interest projected into the image space. Flow goes from left to right.

After projecting physical space into camera space, the intensity values of interest can be extracted for each camera. In order to reduce noise in the reconstructed pressure field, the intensity is averaged over a region of adjacent pixels. It is also beneficial to have one full-field view of the object rather than two separate pressure measurements from both cameras. To address this problem, a blending algorithm was written which takes the intensity fields from both cameras and combines them into one continuous three-dimensional intensity field. After doing so, the intensity field can be converted in pressure using the in-situ calibration constants described above. Since each turret geometry protrudes into the wind tunnel a different amount, the pressure measurements are also corrected to account for varying tunnel blockage by maintaining a constant mass flow rate through the test section.

3.2 Post Processing

3.2.1 Proper Orthogonal Decomposition

Proper Orthogonal Decomposition (POD) is a modal analysis technique that decomposes a data matrix into an optimal basis set of orthogonal spatial modes in order of increasing to decreasing energy. This technique has quickly gained popularity within the fluid mechanics community for a few reasons. Firstly, since POD modes are identified and organized in order of decreasing energy, it quickly becomes apparent what the dominant, or most energetic flow features of a particular environment are. Additionally, since these modes are orthogonal in space, a much lower order data set containing most of the energy can easily be reconstructed. POD will only be introduced here, but much greater detail on this modal technique can be found in Ref. [20]. In this manuscript, POD is used to decompose the measured PSP pressure fields, *p(s,t)*, into orthogonal spatial modes, φ_n, and temporal coefficients, a_n, as seen in Eq. 3.

$$p(s,t) \approx \sum_{n}^{N} a_n(t)\,\varphi_n(s) \tag{3}$$

The modes are found by solving the eigenvalue problem, described in Eq. 4, where *R(s,s')* is the two-point correlation matrix defined as, $R(s,s') = \overline{p(s,t)p(s',t)}$.

$$\int_S R(s,s')\varphi_n(s')ds' = \lambda_n\varphi_n(s) \tag{4}$$

Each mode has associated temporal coefficients. These temporal coefficients are found by taking the inner product of the mode of interest with the pressure matrix, as shown in Eq. 5. These temporal coefficients have the property $\overline{a_n(t)a_m(t)} = \lambda_n\delta_{nm}$.

$$a_n(t) = \int_S p(s,t)\,\varphi_n(s)ds \tag{5}$$

The energy contained within each mode is given by its eigenvalue, which can be computed from the temporal coefficients as $\lambda_n = \overline{a_n^2(t)}$ [15].

3.2.2 Joint Proper Orthogonal Decomposition

The utility of POD has been demonstrated on a wide variety of problems. Since the introduction of this modal analysis technique, variations of traditional POD approaches have also started to arise. Some of these variations include spectral POD (SPOD), temporal POD (TPOD), and joint POD (JPOD) [15, 20, 21.] For the experiments conducted here, JPOD has some particularly useful qualities. The advantage of JPOD is that changes in data due to varying experimental parameters can be more easily identified. For example, in the experiments presented here, four different turret geometries were used. JPOD works by averaging correlation matrices corresponding to data collected from the different parameters, as shown in Eq. 6. Consequently, the JPOD modes are formed from a combined contribution of data from all the included parameters.

$$R_{Joint}(s,s') = \frac{1}{M}\sum_{Params.}^{M} R(s,s',Param) \tag{6}$$

In order to see how much a specific parameter is represented within each mode, the JPOD modes (Φ_n) are projected into the instantaneous pressure field associated with that parameter, as shown in Eq. 7. The resultant energy associated with each mode for a given parameter is given by Eq. 8.

$$a_n(t;\ Param) = \int_S p(s,t;\ Param)\,\Phi_n(s)ds \tag{7}$$

$$\Lambda_n(Param) = \overline{a_n^2(t;Param)} \tag{8}$$

4. RESULTS

Power spectral densities were calculated from pressure measurements collected by the back location Kulite, as well as from PSP pressure values extracted from the turret in proximity to this Kulite location. Representative results are presented in Fig. 7 where the blue line represents the power spectra from the PSP measurements and the red line represents the power spectra from the Kulite measurements. It can be seen that the two are in agreement. The fluctuations in the PSP power spectra can be further minimized by ensemble averaging over a greater number of local spatial points or by analyzing a longer portion of the time series of these spatial points. The resulting pressure fields from the PSP data were converted into pressure coefficients, C_p. The standard deviation of these C_p fields are presented in Fig. 8 as a three-dimensional view, and Fig. 9 as a two-dimensional, respectively. The three-dimensional perspective is viewing the backside of the turret and the two-dimensional view is from the top view of the turret. Each row of plots corresponds to a different turret configuration from least to most protrusion. Each column corresponds to each Mach number tested where Mach 0.3 are the left plots, Mach 0.4 are the middle plots, and Mach 0.5 are the right plots. The high Mach number case for the hemisphere on full cylinder configuration was tested at Mach 0.487 instead of Mach 0.5 due to wind tunnel power restrictions.

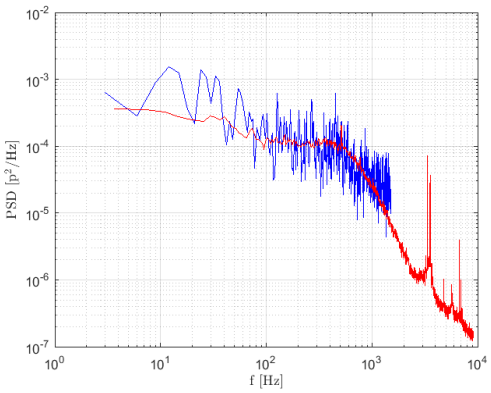

Figure 7. Power spectral density comparison between the back location Kulite and PSP measurements in proximity of this Kulite location.

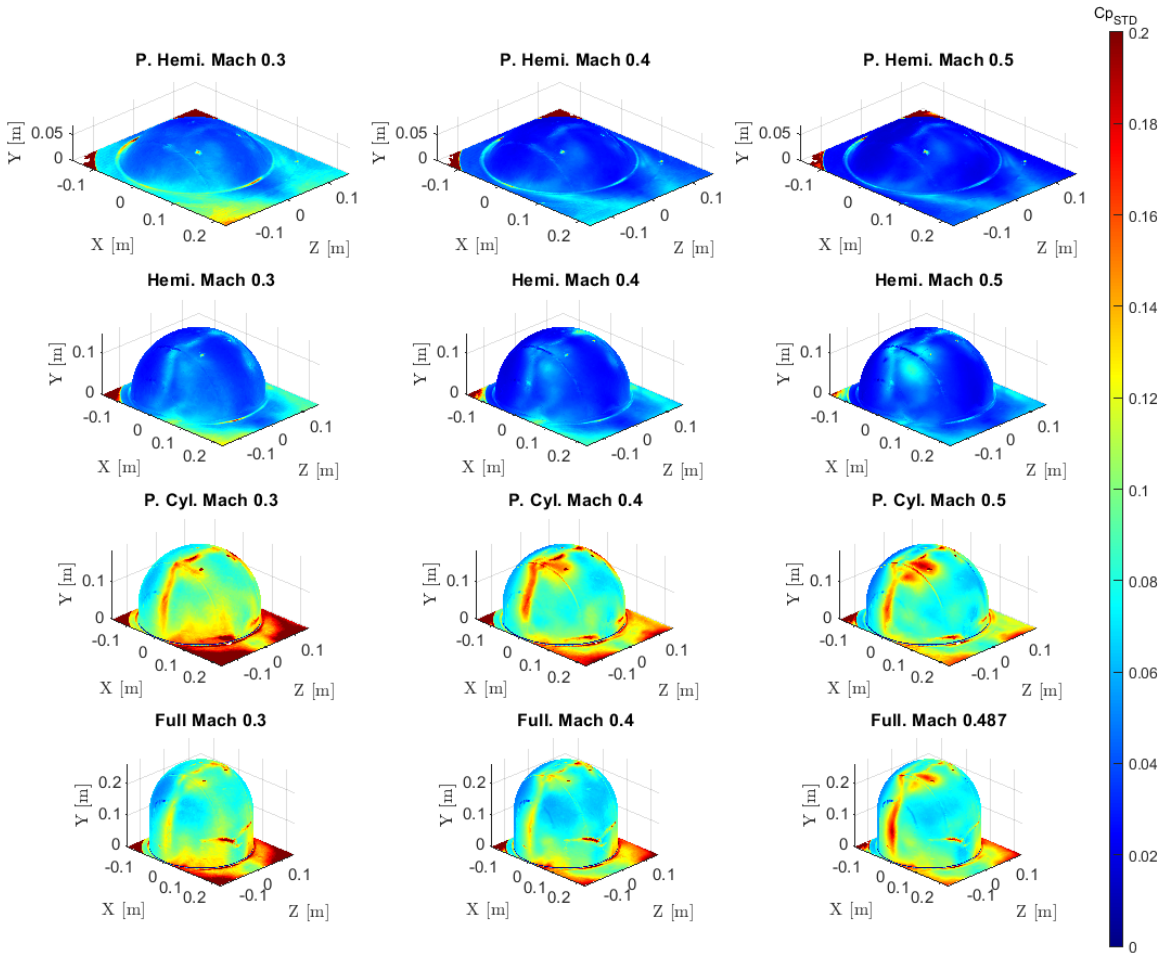

Figure 8. Three-dimensional plots of the pressure coefficient standard deviation surface plots for each configuration and Mach number. Flow goes from left to right.

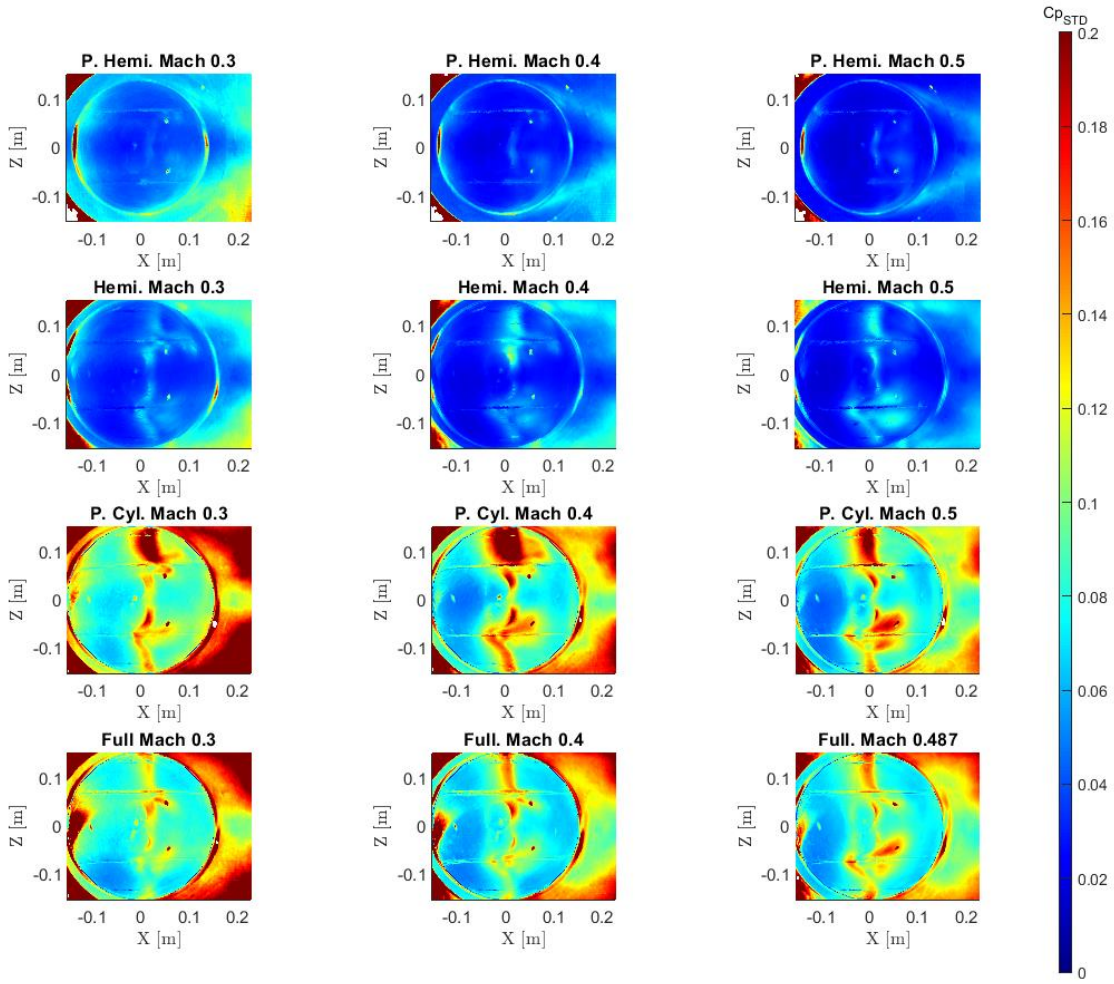

Figure 9. Two-dimensional plots of the pressure coefficient standard deviation surface plots for each configuration and Mach number. Flow goes from left to right.

For the partial hemisphere case, it can be seen that the standard deviation remains fairly constant over the turret surface across all Mach numbers. The standard deviation in the wake region and sides of the turret is notably higher for the Mach 0.3 case compared to the Mach 0.4 and 0.5 case. This is due to a weakened signal to noise ratio by normalizing by the tunnel dynamic pressure. The wake region also reveals pronounced and organized increases in standard deviation on either side of turret angled inwards towards the turret centerline. These standard deviation striations are associated with vortex shedding from the portions of the partial hemisphere away from the centerline. Since the turret is only partially protruding into the flow, there is a small stagnation region on the front of the turret and most of the incoming freestream turbulence structures are able to convect over the top rather than around the sides. The narrow wake, made evident by the increases in standard deviation, is associated with the flow that convects around the sides of the partial hemisphere. For the case of the hemisphere, the standard deviation on the turret surface again looks fairly constant, however now a separation line is clearly visible on the top of the turret. The nonuniformities in the separation line on the turret are likely associated with the realistic turret features such as pressure ports, gaps, and small cavities between different turret components. The wake region of the hemisphere configuration also reveals a higher standard deviation however, the standard deviation of the wake for the hemisphere case is more disorganized than that of the partial hemisphere. This may be associated with a battling between flow convecting over the top versus around the sides of the turret. Additionally, the wake appears to be much wider for the hemisphere case compared to the partial hemisphere case. This likely suggests that for the partial hemisphere case, the flow remains attached longer than for the cases of greater turret protrusion. Despite only being 38

mm different in protrusion distance, the standard deviation surface plot for the hemisphere on partial cylinder configuration looks very different than that of the hemisphere configuration. The standard deviation on the turret surface across all Mach numbers increases drastically compared to the hemisphere and partial hemisphere cases, and the separation line on the top of the turret is also more pronounced. The wake region has a standard deviation that is markedly higher than that of the hemisphere cases. Since some of the cylindrical base is now showing, there is a larger stagnation region on the frontal portion of the turret. Therefore, more turbulent structures are forced to convect around the sides of the turret. It is expected that the strength of the necklace vortex will increase with larger cylindrical base protrusion. The full turret configuration reveals similar phenomena to the hemisphere on partial cylinder case. A higher standard deviation is noticed on the entire surface of the full turret's hemispherical portion and a clear separation line is visible. Again note that the turret used in these tests is not free from imperfections. The pressure turret used here was designed to match a functioning beam director and as such, crevices and pressure ports are scattered across the turret body. These turret qualities create physically small, yet noticeable pressure variations on the turret. It is important to recognize that these pressure field characteristics are not specific to turret geometry, Mach number, or facility but rather the architecture of the turret used for testing here, and they will not be the emphasized of this manuscript.

In order to better identify the dominant features of the local static pressure field acting on the different turret configurations, POD analysis was also employed. The first three POD modes for each turret configuration at Mach 0.4 are presented in Fig. 10. Modes 1 through 3 are presented in the columns of the figure and the different configurations are presented in each row.

For the case of the partial hemisphere presented in the first row of Fig. 10, the first, most energetic mode contains approximately 21% of the total energy and is dominated by uniform surface pressure spatial features. Mode 2, which contains approximately 6.5% of the energy shows some spanwise antisymmetric spatial features. This is an indication that some antisymmetric vortex shedding off the sides of the partial hemisphere may be occurring. The POD modes for the hemisphere case are presented in the second row of Fig. 10. The first and second POD modes show clear spanwise asymmetry and contain 24% and 16.6% of the total energy, respectively. These modes are clearly associated with antisymmetric vortex shedding. Mode 3 is fairly uniform in the streamwise direction and contains approximately 8% of the total energy. It is worth noting that a transition occurs between the partial hemisphere and the hemisphere case. The most energetic POD mode was primarily spanwise symmetric spatial features for the partial hemisphere and the most energetic POD mode for the hemisphere case was dominated by clear antisymmetric spatial surface pressure field characteristics.

The POD modes for the case of the hemisphere on partial cylinder are presented in the third row of Fig. 10. The first mode shows similar spanwise antisymmetric features and contains approximately 42% of the total energy. The second and third mode, containing approximately 15% and 5% of the energy respectively, display symmetric separation line spatial features. The POD modes for the last configuration, hemisphere on full cylinder, are presented in the fourth row of Fig. 10. For this configuration, about 31% of the total energy is contained within the first POD mode. As for the previous configurations, this mode shows the same antisymmetric surface pressure features. The second and third POD modes also display asymmetry about the turret centerline and contain, approximately 19% and 11% of the total surface pressure energy, respectively.

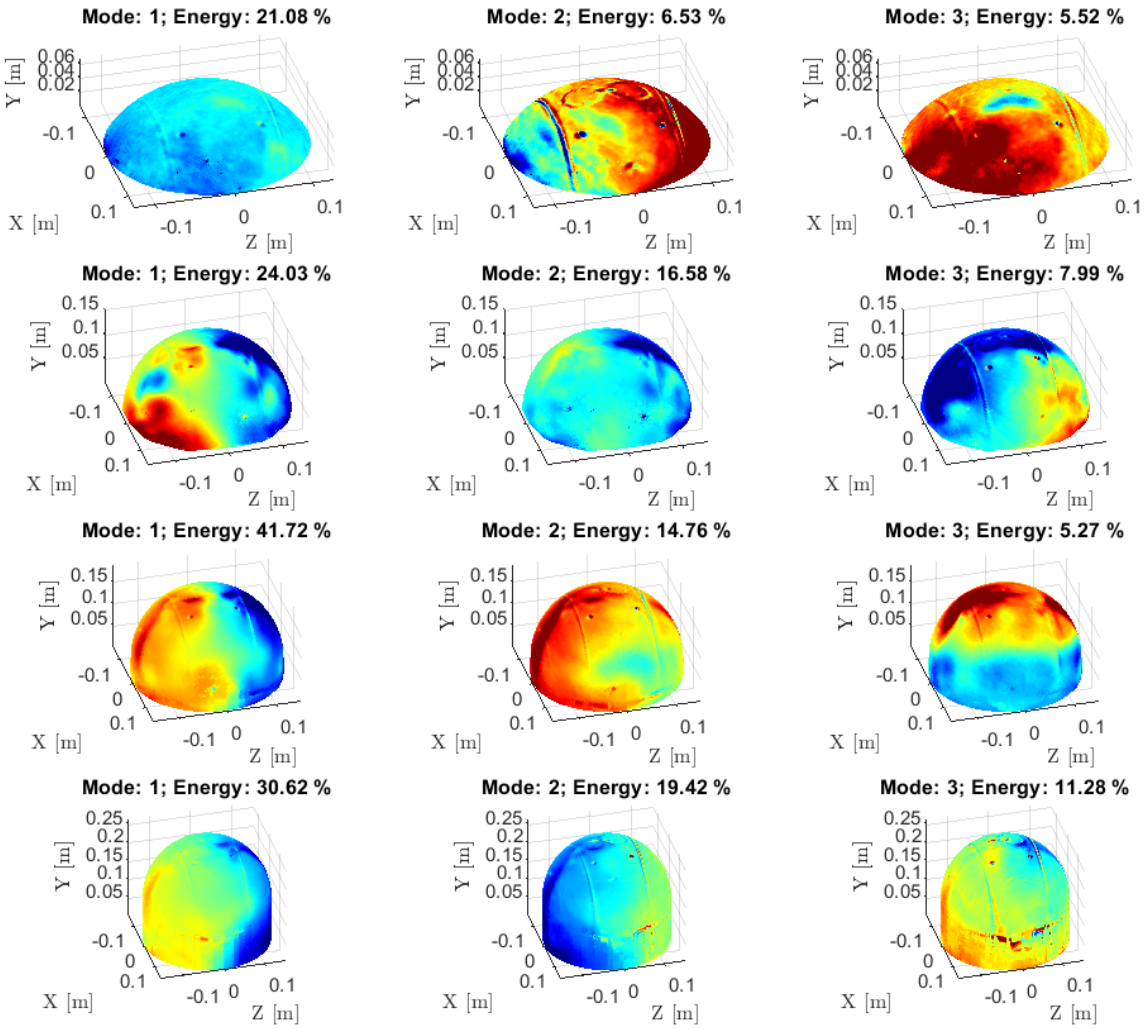

Figure 10. First three POD modes for all turret configurations at Mach 0.4. Flow goes from the top left to bottom right portion of each plot.

From the POD modes presented above, it is apparent that as the turret protrusion into the freestream increases, the energy and prevalence of the spanwise antisymmetric surface pressure field also increases. While these antisymmetric surface pressure features tend to be the most energetic spatial modes for all configurations except the partial hemisphere case, streamwise symmetrical surface pressure spatial features are still present in lower energy POD modes. Figure 11 presents the cumulative sum of the energies associated with the POD modes for each configuration at Mach 0.4. What was evident in the POD modes presented above is also made clear here in Fig. 11. The cases of greater protrusion into the freestream flow tend to require less spatial modes to reconstruct most of the overall energy of the surface pressure field. For the case of the hemisphere on partial cylinder and hemisphere on full cylinder, it requires about 10 POD modes to reconstruct approximately 75% of the total energy whereas for the partial hemisphere case, approximately 100 modes are required to reconstruct the same total energy.

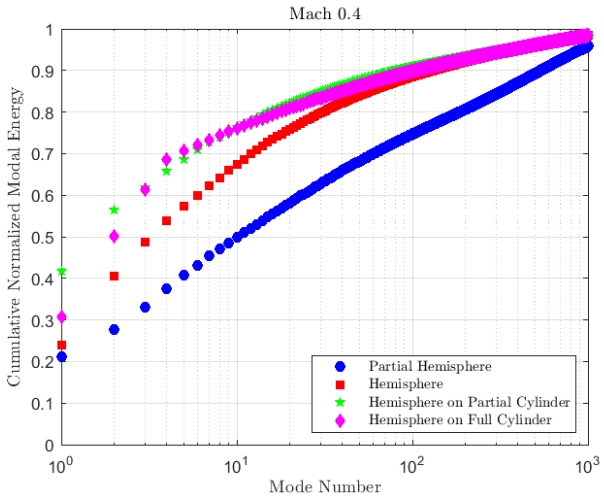

Figure 11. Cumulative normalized modal energies plotted for all configurations at Mach 0.4.

In order to better understand what changes occur with changing protrusion distances, the power spectral densities are computed for the time coefficients of the first three POD modes, for all configurations for the Mach 0.4 case. These results are presented in Fig. 12. The same spectra are also pre-multiplied and plotted against Strouhal number, $St_D = fD/U_\infty$, where D is the turret diameter and U_∞ and is the freestream velocity, in Fig. 13. The spectra are pre-multiplied to more easily be able to visually identify the largest contributing frequencies.

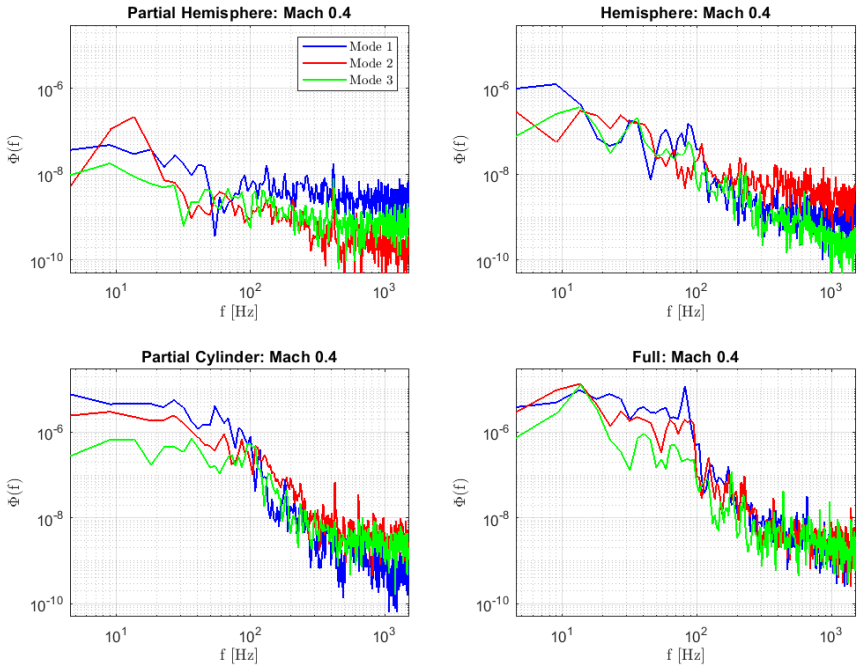

Figure 12. Power spectral densities for the POD time coefficients of the first three modes for all turret configurations at Mach 0.4.

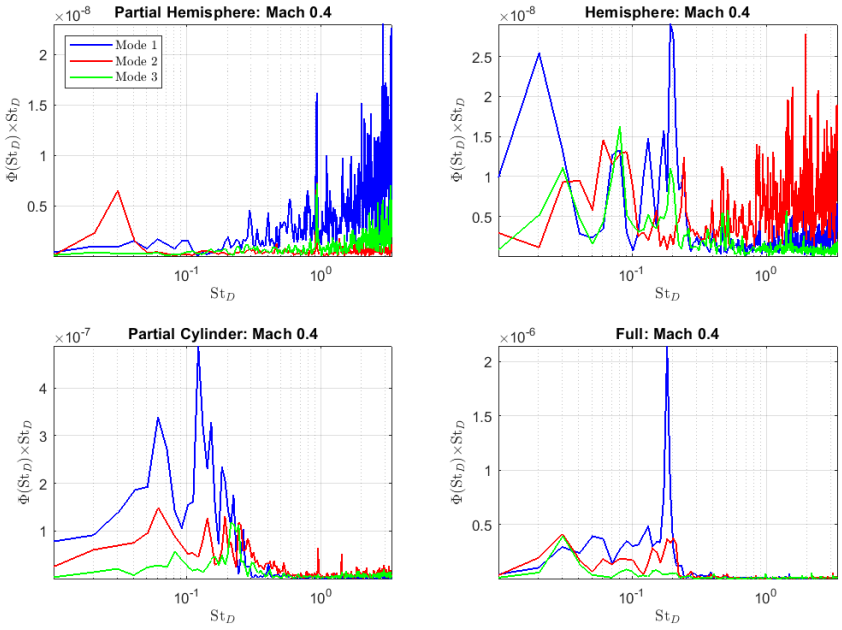

Figure 13. Pre-multiplied and normalized power spectral densities for the POD time coefficients of the first three modes for all turret configurations at Mach 0.4.

For the case of the partial hemisphere, a spectral peak exists at approximately f = 400 Hz or St_D=1 for all of the first three POD modes. This peak may be associated with the shedding frequency of the shear-layer structures which convect over the top of the turret. Besides this peak, the first three POD modes consist of broadband energy contribution, which is expected since visually, the POD modes presented in Fig. 10 did not have any overly dominant spatial features. Additionally, the cumulative modal energies presented in Fig. 11 demonstrated that it requires a large number of POD modes to sufficiently resolve the partial hemisphere surface pressure environment. For the case of the hemisphere, a dominant spectral peak associated with the spectra for the first POD mode can be seen at St_D=0.2. This is in agreement with the spanwise antisymmetric shedding frequency observed in literature. For the case of the partial cylinder, the spectral peak at St_D=0.2 is still present however there exists another large peak at St_D=0.13 and St_D=0.06. For the case of the hemisphere on full cylinder, the first POD is almost entirely summarized by the spectral peak at St_D=0.2.

Since a portion of the wake was also imaged for all configurations, JPOD was employed to investigate the wake dynamics associated with different turret protrusion. Figure 14 presents the first six JPOD modes calculated with the Mach 0.4 case for each configuration. Here, the x-axis represents the streamwise location and the y-axis represents the spanwise location. It can very clearly be seen that the first mode is dominated by spanwise antisymmetric surface pressure features about the streamwise centerline whereas the second mode reveals symmetric surface pressure spatial features. Modes three through six all display higher order surface pressure spatial features. By projecting the JPOD mode into the instantaneous pressure field associated with each configuration, the prevalence of each mode amongst the different configurations can be analyzed. In order to do so, the power spectral densities of the JPOD time coefficients associated with each configuration are then computed. These results are plotted in Fig. 15 as power spectral density versus normalized frequency. The spectra for the first mode reveal a strong peak at St_D=0.2 which increases in strength with increasing turret protrusion. This peak is highlighted in Fig. 15 a yellow rectangle. For the minimally protruding partial hemisphere case, this peak is essentially absent. This confirms a fundamental change in wake dynamics between the minimally protruding partial hemisphere and the hemisphere case. The spectra for the second mode reveals a pronounced peak at St_D=1, highlighted by a red arrow in Fig. 15. This peak was also noticed in the spectra of the POD time coefficients presented in Figs. 12 and 13. This peak is evident for all configurations but it is particularly apparent for the partial hemisphere. For an overall less energetic partial hemisphere case within the first six JPOD modes, the spectral peak at St_D=1 is strong when compared to the other

configurations. This may indicate that this frequency is related to the symmetric shedding resulting from flow convecting over the top of the turret. Modes three through six reveal more complicated wake phenomena however the spectra reveals that these spatial features are only majorly present in cases of greater protrusion. The spectra of the JPOD time coefficients for the partial hemisphere case reveals that modes three through six are minimally associated with the wake dynamics of the partial hemisphere. The wake dynamics noticed in modes three through six may be resultant from the necklace and secondary vortices which are likely either absent or weak for the partial hemisphere case.

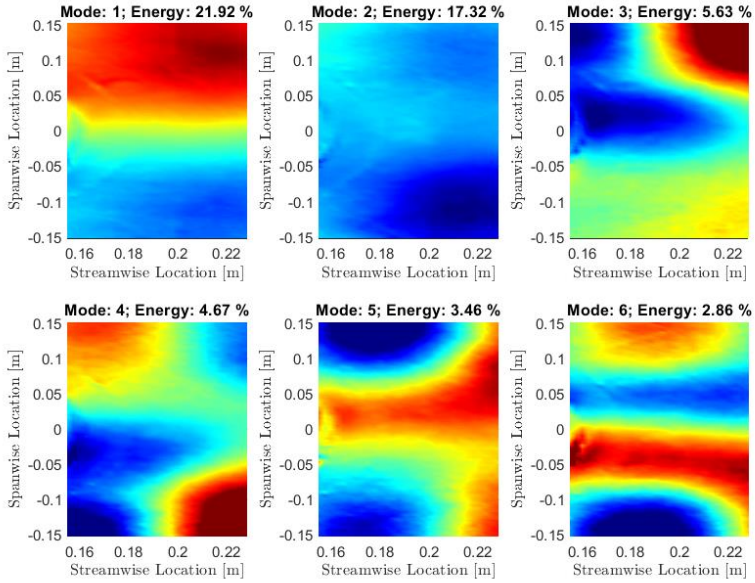

Figure 14. First six JPOD modes calculated on the wake for all configurations for the Mach 0.4 case.

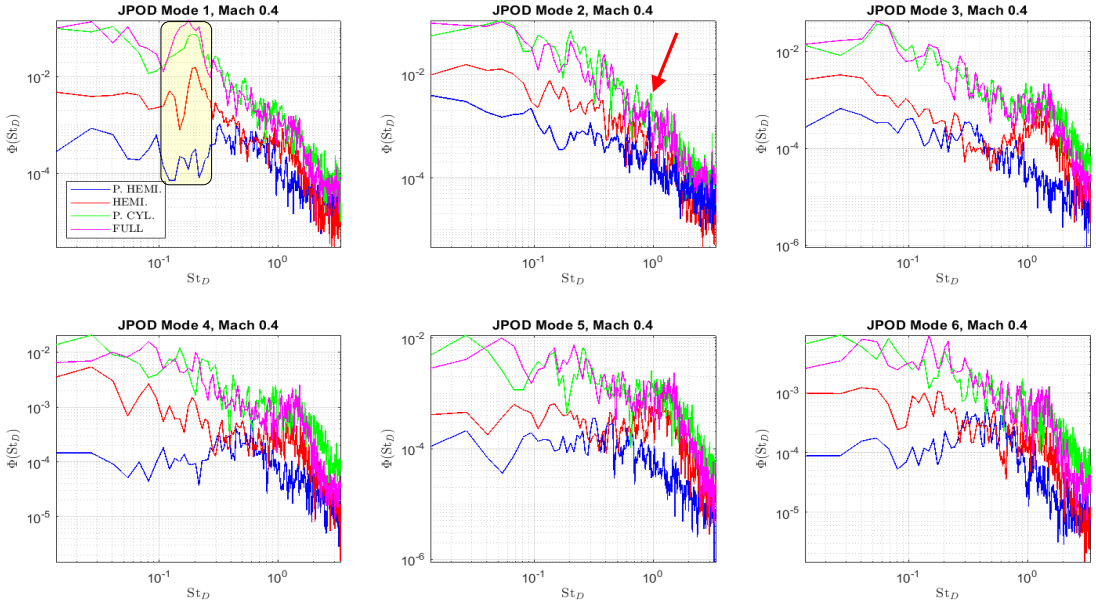

Figure 15. Power spectral density plotted versus Strouhal number for the time coefficients of the first six JPOD modes of the wake region for each turret configuration at Mach 0.4.

Since this work is concerned with investigating how the surface pressure field is acting on the turret for various geometries and Mach numbers, it is straightforward to extend the analysis to calculate what the resultant net forces are acting on the turret[22]. By integrating the surface pressure field over the turret, a resultant net force can be calculated as described by, $F_i = \int_{SA} p_i \cdot u_i dA$, where p is the surface local static pressure field, and u_i is the unit inward normal vector. For each turret configuration, the pressure field is discretized using a Delaunay triangulation. The area and unit vector of each local triangle on the turret surface is calculated. A simplified visual of this is presented in Fig. 16. Figure 17 presents the normalized rms net force calculated over the turret for each turret configuration and Mach number. The net force is normalized by dynamic pressure and the cross-sectional area of the turret. Only the normalized net force results acting in the spanwise direction are presented. Since two cameras were used to extract three-dimensional surface pressure measurements around the turret and the wake, sides, and backside of the turret were the primary regions of interest, the front and top of the turret were not imaged sufficiently to make accurate net force calculations in the streamwise and wall normal direction. Generally, in the spanwise direction, the greater the protrusion, the more net force imposed onto the turret. The spanwise antisymmetric shedding, discussed in this manuscript, is the most probable cause for the higher normalized net force in the spanwise direction at larger turret protrusions. The partial hemisphere configuration has minimal spanwise net force since there was minimal unsteady forcing acting in this direction.

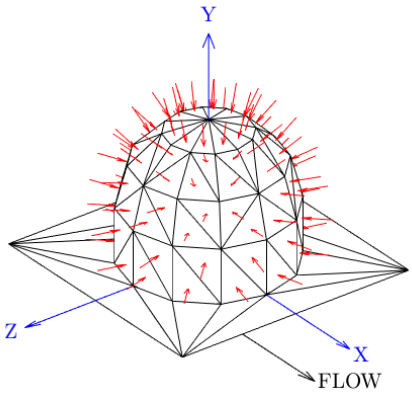

Figure 16. Simplified visualization of Delaunay triangulation on the turret surface with unit vectors.

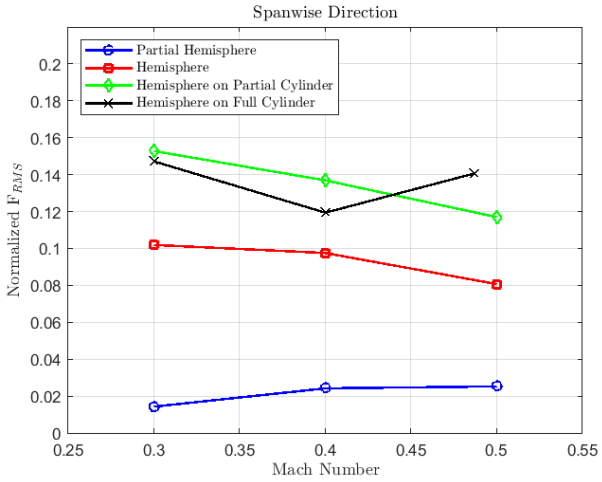

Figure 17. Normalized force rms calculated on the turret pressure field for each configuration and all Mach numbers in both the streamwise and spanwise directions.

5. CONCLUSIONS

Wind tunnel surface pressure measurements using fast-response pressure sensitive paint were taken on a hemisphere-on-cylinder turret at various protrusion distances and Mach numbers. This parametric study was conducted in order to better understand the characteristics of the unsteady pressure field on the backside and wake of the turret. Proper orthogonal decomposition was used to identify the dominant spatial surface pressure modes acting on the turret and spectra was computed on the proper orthogonal decomposition temporal coefficients to identify relevant surface pressure frequencies acting on the turret. The further the turret protruded into the freestream flow, the greater the presence of spanwise antisymmetric surface pressure distribution. This spanwise anti-symmetrical surface pressure distribution results from antisymmetric vortex shedding at a normalized frequency of St_D=*0.2*. By calculating the cumulative POD mode energy for each turret configuration, it was found that fewer modes were required to reconstruct a large percentage of total surface

pressure energy for the greater turret protrusion cases. For the case of the partial hemisphere, the spanwise anti-symmetrical vortex shedding was majorly absent, insinuating that at some protrusion distance, the surface pressure environment on the turret fundamentally changes. Net force calculations for all Mach number and turret configurations were performed. It was found that as turret protrusion distance increases, so does the spanwise net force acting on the turret, confirming the findings established in the POD results.

ACKNOWLEDGEMENTS

This work is supported by the Air Force Research Lab, Cooperative agreement number FA9451-17-2-0088. The U.S. Government is authorized to reproduce and distribute reprints for governmental purposes notwithstanding any copyright notation thereon.

DISCLOSURES

Approved for public release; distribution is unlimited. Public Affairs release approval number # AFRL-2021-2267.

REFERENCES

[1] Savory E, Toy N, "The flow regime in the turbulent near wake of a hemisphere," Experiments in Fluids, 4, 181–188. doi.org/10.1007/BF00717812 (1986).
[2] Tavakol MM, Abouali O, Yaghoubi M, "Large eddy simulation of turbulent flow around a wall mounted hemisphere," Applied Mathematical Modelling 39(13), 3596–3618. doi.org/10.1016/j.apm.2014.11.055, (2015).
[3] Manhart M, "Vortex shedding from a hemisphere in a turbulent boundary layer," Theoretical and Computational Fluid Dynamics 12(1), 1–28. doi.org/10.1007/s001620050096 (1998).
[4] Wood JN, De Nayer G, Schmidt S, and Breuer M, "Experimental investigation and large– eddy simulation of the turbulent flow past a smooth and rigid hemisphere," J. Flow, Turbulence and Combustion 97 (1), 79–119. doi.org/10.1007/s10494-015-9690-5 (2016).
[5] Gordeyev S and Jumper E, "Fluid Dynamics and Aero-Optics of Turrets," *Progress in Aerospace Sciences*, 46, pp. 388-400. doi.org/10.1016/j.paerosci.2010.06.001 (2010).
[6] Vukasinovic B, Glezer A, Gordeyev S, Jumper E and Bower WW, "Flow Control for Aero-Optics Application," Experiments in Fluids, 54, 1492. doi:10.1007/s00348-013-1492-8 (2013).
[7] De Lucca N, Gordeyev S, Morrida J and Jumper EJ, "Investigation of Flow Dynamics Over Turrets with Different Spanwise Aspect Ratios Using PSP," AIAA Paper 2018-2047 (2018a).
[8] De Lucca N, "Studies of the Pressure Field and Related Beam Jitter for Hemisphere-on-Cylinder Turrets," PhD thesis, University of Notre Dame (2015).
[9] Matthews E, Wang K, Wang M and Jumper E, "LES of an Aero-Optical Turret Flow at High Reynolds Number," AIAA 2016-1461 (2016).
[10] Morrida, J, Gordeyev S and Jumper E, "Transonic Flow Dynamics Over a Hemisphere in Flight," AIAA Paper 2016-1349 (2016).
[11] Porter C, Gordeyev S, Zenk M and Jumper E, "Flight measurements of the Aero-Optical Environment around a Flat-Windowed Turret," AIAA Journal, 51(6), 1394-1403. doi.org/10.2514/1.J052067 (2013).
[12] Ladd J, Mani A and Bower W, "Validation of Aerodynamic and Optical Computations for the Unsteady Flow Field About a Hemisphere-on-Cylinder Turret," AIAA Paper 2009-4118 (2009).
[13] Coirier WJ, Porter C, Barber J, Stutts J, Whiteley M, Goorskey D, and Drye R, "Aero-Optical Evaluation of Notional Turrets in Subsonic, Transonic and Supersonic Regimes" AIAA Paper 2014-2355 (2014)
[14] Jelic R, Sherer S and Greendyke R, "Simulation of Various Turret Configurations at Subsonic and Transonic Flight Conditions Using OVERLOW," Journal of Aircraft 2013 50:2, 398-409. doi.org/10.2514/1.C031844 (2013).
[15] Gordeyev S, De Lucca N, Jumper EJ, Hird K, Juliano TJ, Gregory JW, Thordahl J, and Wittich DJ, "Comparison of unsteady pressure fields on turrets with different surface features using pressure-sensitive paint," Exp Fluids, 55, 1661. doi.org/10.1007/s00348-013-1661-9 (2014).
[16] Hayashi T and Sakaue H, "Temperature Effects on Polymer-Ceramic Pressure-Sensitive Paint as a Luminescent Pressure Sensor," Aerospace. 7(6):80. doi.org/10.3390/aerospace7060080 (2020).

[17] S Sakaue H, Kakisako T, Ishikawa H., “Characterization and optimization of polymer-ceramic pressure-sensitive paint by controlling polymer content.,” Sensors (Basel). 2011;11(7):6967-77. doi: 10.3390/s110706967. Epub 2011 Jul 4. PMID: 22163996; PMCID: PMC3231655.
[18] Carlbom I, Paciorek J, “Planar geometric projections and viewing transformations,” ACM Comput Surv 10(4):465–502 (1978).
[19] Haralick RM, “Using perspective transformations in scene analysis,” Comput Graph Image Process 13:191–221 (1980).
[20] Taira K, Brunton SL, Dawson STM, Rowley CW, Colonius T, McKeon BJ, Schmidt OT, Gordeyev S, Theofilis V, and Ukeiley LS, “Modal Analysis of Fluid Flows: An Overview,” AIAA Journal, 55(12), 4013–4041. doi.org/10.2514/1.J056060 (2017).
[21] Gordeyev & Thomas, "A Temporal Proper Decomposition (TPOD) for Closed-Loop Flow Control", Experiments in Fluids, 54, (2013).
[22] De Lucca N, Gordeyev S, Jumper EJ, Hird K, Juliano TJ, Gregory JW, Thordahl J and Wittich DJ, “The Estimation of the Unsteady Aerodynamic Force Applied to a Turret in Flight,” AIAA Paper 2013-3136, (2013).